Bioconjugate Chemistry

pubs.acs.org/bc Article

NIR Fluorescent Imaging and Photodynamic Therapy with a Novel Theranostic Phospholipid Probe for Triple-Negative Breast Cancer Cells

Natalia I. Rubtsova, Michael C. Hart, Alejandro D. Arroyo, Sofya A. Osharovich, Benjamin K. Liebov, Joann Miller, Min Yuan, Jeffrey M. Cochran, Sanghoon Chong, Arjun G. Yodh, Theresa M. Busch, E. James Delikatny, Nadia Anikeeva, and Anatoliy V. Popov*

Cite This: *Bioconjugate Chem.* 2021, 32, 1852−1863 Read Online

ACCESS | Metrics & More | Article Recommendations | Supporting Information

ABSTRACT: New exogenous probes are needed for both imaging diagnostics and therapeutics. Here, we introduce a novel nanocomposite near-infrared (NIR) fluorescent imaging probe and test its potency as a photosensitizing agent for photodynamic therapy (PDT) against triple-negative breast cancer cells. The active component in the nanocomposite is a small molecule, pyropheophorbide *a*-phosphatidylethanolamine-QSY21 (Pyro-PtdEtn-QSY), which is imbedded into lipid nanoparticles for transport in the body. The probe targets abnormal choline metabolism in cancer cells; specifically, the overexpression of phosphatidylcholine-specific phospholipase C (PC−PLC) in breast, prostate, and ovarian cancers. Pyro-PtdEtn-QSY consists of a NIR fluorophore and a quencher, attached to a PtdEtn moiety. It is selectively activated by PC−PLC resulting in enhanced fluorescence in cancer cells compared to normal cells. In our *in vitro* investigation, four breast cancer cell lines showed higher probe activation levels than noncancerous control cells, immortalized human mammary gland cells, and normal human T cells. Moreover, the ability of this nanocomposite to function as a sensitizer in PDT experiments on MDA-MB-231 cells suggests that the probe is promising as a theranostic agent.

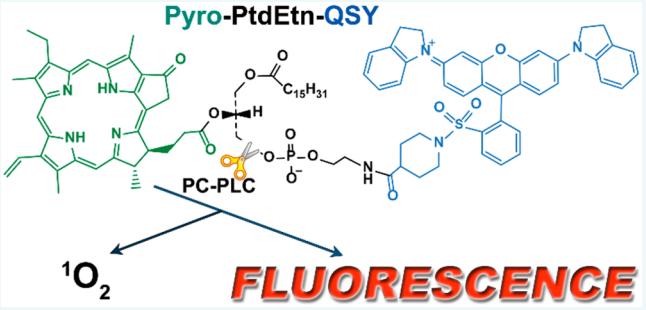

INTRODUCTION

Triple negative breast cancers (TNBC) are heterogeneous tumors that share common phenotypic features: low expression of the estrogen receptor, progesterone receptor, or human epidermal growth factor receptor 2 (HER2). TNBC are associated with poor prognosis and overall survival.[1] Since TNBC lacks most common biomarkers of breast cancers, the options for detection and therapy are limited, and novel molecular targets are urgently needed.[2]

Despite the incredible genetic and histological heterogeneity of tumors, malignancy seems to involve the common induction of a finite set of metabolic pathways to support core functions.[3] Because many cancers exhibit altered lipid metabolism, it is possible to develop imaging probes, targeting specific enzymes in these pathways. Abnormal choline metabolism has known associations with oncogenesis and tumor progression[4,5] leading to elevated levels of phosphocholine (PC) in prostate,[6−10] brain,[6,8,11−14] ovarian,[15−21] and breast[6,11,22−26] cancer cells and solid tumors. Multiple metabolic pathways lead to PC production, including the anabolic phosphorylation of choline by choline kinase and the catabolism of phosphatidylcholine by PC−PLC.[27−34] The contribution of PC−PLC to PC production was estimated to be between 20% and 50% in breast cancer and ovarian cancer cell lines.[16,20] The activity of the enzyme increased 2- to 6-fold and was associated with a similar elevation of PC−PLC protein expression compared to immortalized noncancerous cells.[21,35] Immunohistochemical examinations of epithelial ovarian cancer sections revealed high levels of PC−PLC in 87% of samples.[21] PC−PLC overexpression is accompanied by subcellular redistribution of the enzyme to the plasma membrane and/or the perinuclear compartment leading to further enrichment of the enzyme in subcellular compartments by up to 17-fold.[17] Translocation of PC−PLC to subcellular compartments is associated with the overexpression of EGFR and metastatic markers such as HER2 in breast and ovarian cancer cells and beta-1 integrin in epithelial ovarian cancer cells.[21,36] Inhibition of PC−PLC led

Received: June 1, 2021
Revised: June 4, 2021
Published: June 17, 2021

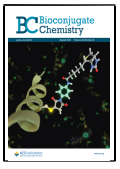

https://doi.org/10.1021/acs.bioconjchem.1c00295
Bioconjugate Chem. 2021, 32, 1852−1863

to impaired cancer cell proliferation.[19,37] In highly metastatic TNBC cells, inhibition of PC−PLC was also accompanied by increased differentiation and decreased migration and invasion.[35] It has been suggested that PC−PLC is involved in controlling the molecular pathways responsible for maintaining a mesenchymal-like phenotype in metastatic breast cancer cells. Recent data have shown that the inhibition of PC−PLC activity selectively affects the most aggressive and tumor promoting subpopulation of squamous cancer cells possessing different proliferative and stemness potential.[37] These data indicate that PC−PLC may be an effective target for breast cancer therapy, particularly for tumors with high metastatic potential.

We have developed smart near-infrared (NIR) fluorescent phospholipid probes that fluoresce after selective cleavage by PC−PLC.[27,29,38] Smart probes that only fluoresce upon enzymatic activation specific to malignant cells are currently at the forefront of cancer imaging research, offering potential for improved selectivity.[10−15] PC−PLC shows a high degree of selectivity to phosphatidylcholine (PtdCho) and phosphatidylethanolamine (PtdEtn) when a bulky substituent is attached to the *sn*-2 position of these phospholipids.[27−29] This principle is exploited in our probe, pyropheophorbide *a*-phosphatidylethanolamine-QSY21 (Pyro-PtdEtn-QSY, Figure 1a), which is selectively cleaved in the presence of PC−PLC.[38]

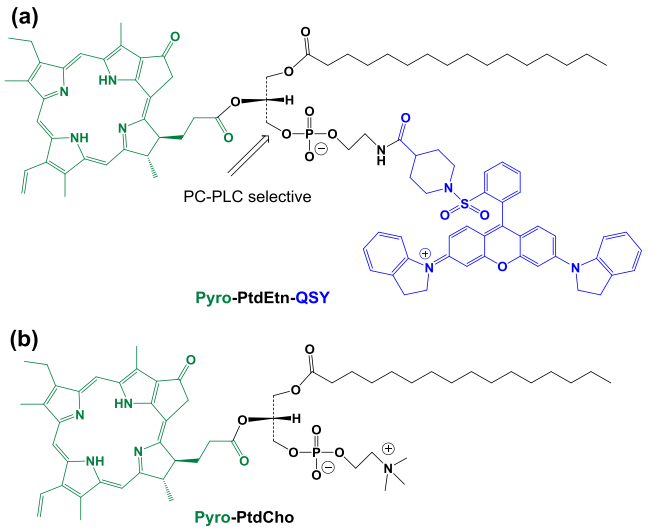

Figure 1. Phospholipid NIR fluoroprobes: (a) quenched Pyro-PtdEtn-QSY; (b) permanently fluorescent Pyro-PtdCho.

Pyro-PtdEtn-QSY has a PtdEtn core, substituted with a bulky pyropheophorbide *a* (Pyro) fluorophore at the *sn*-2 position, as well as a quencher moiety attached to the phosphate headgroup of the phospholipid, designed to suppress the fluorescence until the probe is cleaved. Pyro is a NIR fluorophore (λ_{abs} = 670 nm, λ_{em} = 720 nm) with well-established photosensitizing properties. Absorption of NIR light by the fluorophore induces production of singlet oxygen with high quantum yield making the probes useful for PDT.[39−41] The reactive oxygen species released in this process can selectively kill cancer cells. Thus, in addition to its potential role as a diagnostic tool, the probe can also be used as a PDT therapy agent. QSY21 has been selected as the quencher of choice for this study. A variety of activatable smart probes incorporating QSY21 have been reported, targeting various biological processes.[42−56]

Here, the imaging and therapeutic potential of the probe was evaluated in a series of *in vitro* experiments. To deliver the probe to cells, we incorporated Pyro-PtdEtn-QSY into lipid-based nanoparticles (LNPs) as carriers. Full quenching of the probe prior to PC−PLC activation was confirmed by the absorbance and fluorescence spectra of LNPs, incorporating Pyro-PtdEtn-QSY and pyropheophorbide *a*-phosphatidylcholine (Pyro-PtdCho, a nonquenched positive control probe, Figure 1b). Probe uptake and activation levels in various types of cells were obtained from flow cytometry experiments, and the kinetics of activation were explored. The specificity of the probe activation was evaluated using a PC−PLC inhibitor. Activated fluorophore localization and the overall feasibility for imaging were addressed in live cell microscopy experiments. Diffuse optical tomography (DOT) was utilized to determine the depth to which the fluorophore can be detected in a breast phantom. Finally, the therapeutic potential of the probe was assessed by measuring the dark toxicity of the probe and then by performing PDT experiments, which include cell proliferation and colony formation assays following irradiation with light.

RESULTS AND DISCUSSION

Pyro-PtdEtn-QSY and Pyro-PtdCho were synthesized following procedures reported previously (Schemes S1, S2).[38,57−59] In earlier studies, NIR Black Hole Quencher-3 (BHQ-3, absorbance range 620−730 nm) had been incorporated into the structure of the quenched probe.[27−29] The BHQ-3 quencher fully absorbed the fluorescence emitted by Pyro through Förster resonance energy transfer (FRET).[27] Pyro-PtdEtn-BHQ showed successful activation in DU145 human prostate cancer cells;[27−29] however, BHQ-3 has experienced stability problems *in vivo* due to the presence of an azo bond in the structure.[42,60−62] Complicated synthesis and short shelf life make its use impractical for clinical applications, and as a result, a more stable quencher is required. QSY21 has a similar quenching range (580−720 nm), but does not contain an azo bond and proves to be more stable.[38,63]

Pyro-PtdEtn-QSY is a modified lipid. In order to be activated, the probe has to intercalate into the tumor cell membrane. The nature of our probe requires the use of a lipophilic carrier that delivers the probe to the cancer cell membrane. Lipid-based nanoparticles (LNPs), such as liposomes and micelles, are ideally suited for this purpose.[64] To deliver our PDT probe, we utilized lipid micelles with polyethylene glycol-phosphatidylethanolamine (PEG-PtdEtn) conjugate as a major constituent.[65] The hydrophilic PEG prevents adsorption of proteins and cells, decreasing *in vivo* removal of the particles from circulation by the reticuloendothelial system.[66] Due to their small size, LNPs should have low immunogenicity compared to large PEGylated liposomes.[67,68] For cell delivery, nanoparticles loaded with 13.5 mol % of either Pyro-PtdEtn-QSY or Pyro-PtdCho were prepared using an established protocol;[38] the complete procedure is provided in the Experimental Section. Nanoparticle size distribution was determined by dynamic light scattering, using nanoparticles that did not carry the photosensitizer; these micelles had uniform size with diameter of 10.8 ± 2.9 nm (Figure S1), in agreement with our previous results.[65]

Quenching efficiency was evaluated by comparing the absorbance and fluorescence spectra of the micelles carrying

https://doi.org/10.1021/acs.bioconjchem.1c00295
Bioconjugate Chem. 2021, 32, 1852−1863

Pyro-PtdEtn-QSY and Pyro-PtdCho (Figures 2 and 3). As is evident from the fluorescence spectrum (with 665 nm

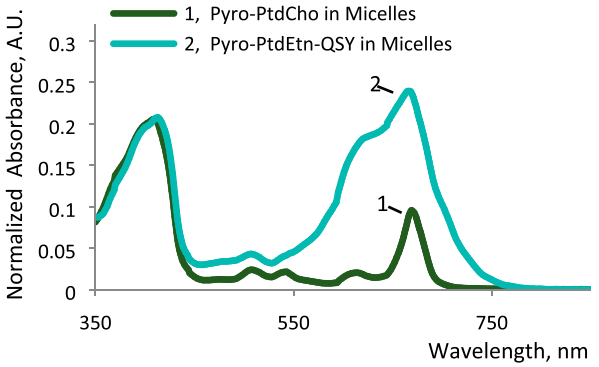

Figure 2. Absorbance of micelles containing 13.5 mol % Pyro-PtdCho and Pyro-PtdEtn-QSY in HEPES buffer, total photosensitizer concentration, 2.36 μM.

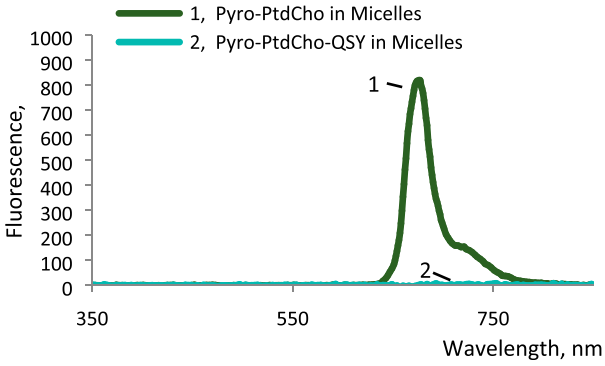

Figure 3. Fluorescence of micelles containing 13.5 mol % Pyro-PtdCho or Pyro-PtdEtn-QSY following 665 nm excitation, measured in HEPES buffer at total photosensitizer concentration 2.36 μM.

excitation), full quenching is achieved in Pyro-PtdEtn-QSY micelles. This indicates that any pyropheophorbide *a* acid impurity, as observed earlier,[38] was excluded in the micelle formation process, likely due to the lack of the lipid backbone in Pyro molecule's structure.

To evaluate probe activation *in vitro*, we utilized breast cancer cell lines of different subtypes, including triple-negative basal-like EGFR-positive MDA-MB-231, triple-negative luminal androgen receptor positive MDA-MB-453, HER2-positive SKBR-3, and estrogen receptor positive MCF-7 cells. Non-tumorigenic mammary epithelial cells MCF-12A and CD8 T cells were used as negative controls.

Fluorophore activation levels in different cell lines were quantified in a series of flow cytometry experiments (Figure 4), in which cells were incubated with 1 μM Pyro-PtdEtn-QSY nanoprobe for 6 h, and the average fluorescence of individual cells was determined. The cancer cells (blue, purple, and magenta bars) exhibited a 2- to 6-fold increase in probe activation levels, compared to noncancerous control cells (green bars). The highest probe activation occurred in MDA-MB-231 cells, followed by the MDA-MB-453 and SKBR-3 cell lines. These results are in agreement with previous studies by Podo's group where PC−PLC accumulation and activity were studied using custom-made polyclonal antibodies and with an Amplex Red PC−PLC assay.[35,36,69] The activity of PC−PLC was significantly higher in triple negative breast cancer lines

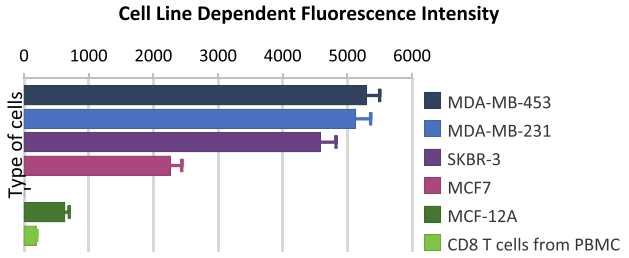

Figure 4. Extent of Pyro-PtdEtn-QSY probe activation in different cell lines as measured by flow cytometry. Cells were incubated with 1 μM of the probe for 6 h. Each experimental value represents the mean of three independent experiments. Standard deviations are indicated for each mean as error bars.

MDA-MB-231 and MDA-MB-453 compared to MCF-7 cells. Nontumoral cells possessed the lowest level of PC−PLC activity compared to breast cancer lines. To verify this correlation, we determined PC−PLC activity in the breast cancer cell lines using an Amplex Red PC−PLC Assay (Sigma). Analysis of PC−PLC activity in total cell lysates confirmed that TNBC cell lines, MDA-MB-231 and MDA-MB-453, have approximately 2-fold increased activity of PC−PLC compared to the estrogen-receptor-positive MCF-7 line (Figure S2).

The ability of breast cancer cell lines to accumulate fluorescence may also depend on the rate of the probe uptake. TNBC cell lines may possess increased uptake of nanoprobes. To assess the effects of cellular uptake, breast cancer cell lines were treated with a nonquenched fluorescent Pyro-PtdCho nanoprobe. For all tested cell lines, the fluorescence arising from Pyro-PtdCho incubation was marginal and roughly an order of magnitude lower than the fluorescence from cells treated with the Pyro-PtdEtn-QSY probe (Table S1). This could have occurred for any of the following reasons: (1) Pyro-PtdCho-loaded nanoparticles have a net negative charge resulting in repulsion from negatively charged cell membranes; (2) lipid exchange between the Pyro-PtdCho nanoparticles and the cell membranes is slow; (3) Pyro-PtdCho cannot be incorporated into the cell membrane; (4) Pyro-PtdCho is not a substrate for PC−PLC. However, the fact that only the PC−PLC specific Pyro-PtdEtn-QSY probe can cross the cell membrane would be of benefit for *in vivo* imaging; impurities or degradation products involving pyropheophorbide *a* or Pyro-PtdCho moieties would remain extracellular and carried away with blood flow *in vivo*.

To elucidate the effects of cellular uptake on fluorescence, we have developed nanoparticles containing both activatable Pyro-PtdEtn-QSY probe and nonactivatable permanently fluorescent (TopFluor) AF488 (1,2-distearyl-*sn*-glycero-3-phosphoethanolamine-*N*; PtdEtn-AF488, λ_{ex} = 488 nm, λ_{em} = 519 nm) lipids at 13.5 and 3 mol % correspondingly (Figure S3a). Two breast cancer cell lines MCF-7 and MDA-MB-231 with different levels of PC−PLC activity were tested. The cellular probe uptake[70−72] was measured using Alexa Fluor 488 fluorescence, while probe activation was measured using Pyro fluorescence (Figure S3b). Probe uptake was slightly higher in MDA-MB-231 cells than in MCF-7 cells (Figure S3c), calculated in molecules of equivalent soluble fluorochrome (MESF) units using calibrated AF488 fluorescent beads. The probe activation level was normalized relative to probe uptake. We found that the probe was activated more efficiently in MDA-MB-231 cells than in MCF-7 cells even after correction

https://doi.org/10.1021/acs.bioconjchem.1c00295
Bioconjugate Chem. 2021, 32, 1852−1863

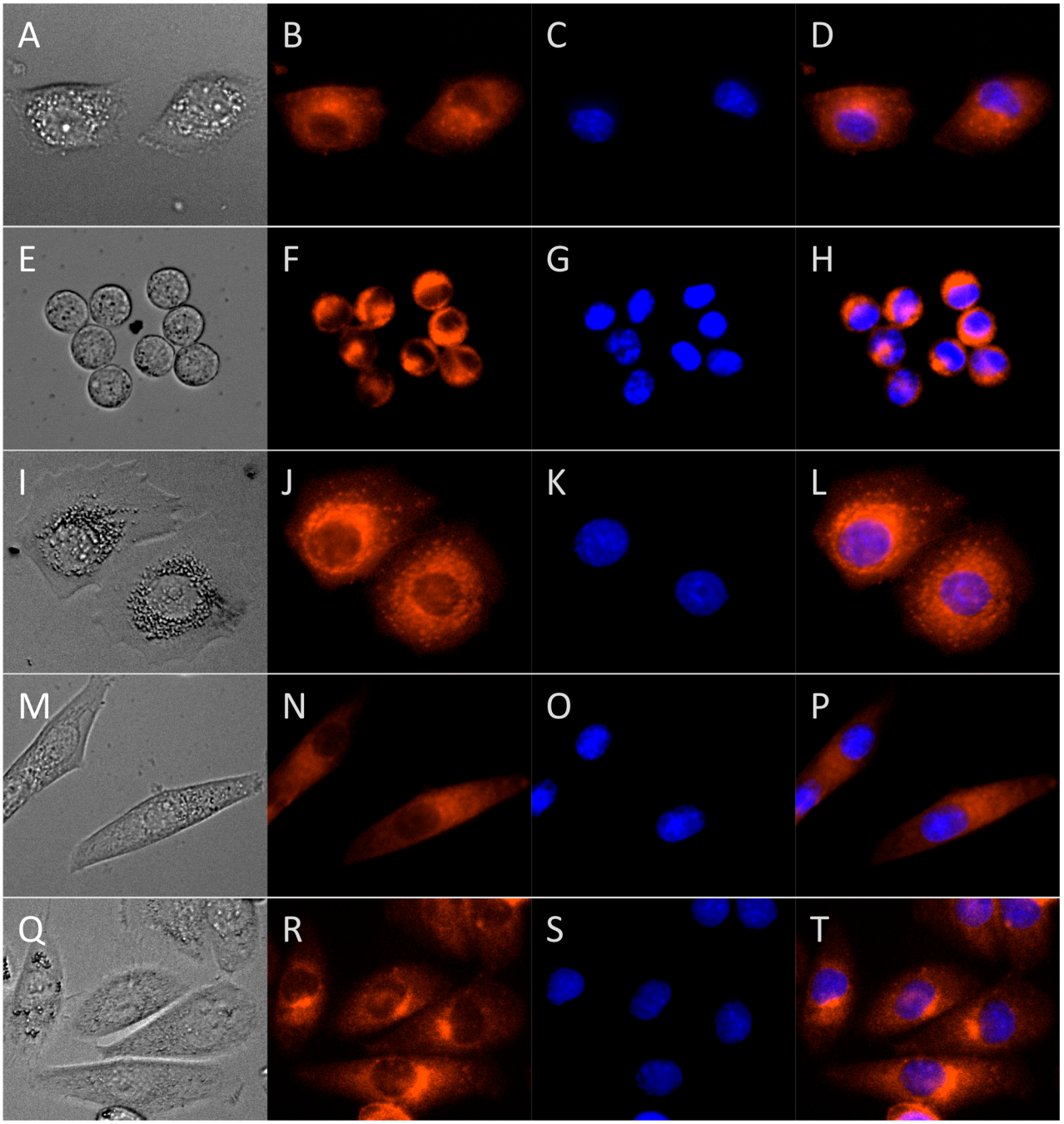

Figure 5. Live cell microscopy images, 40× magnification, stained by the Pyro-PtdEtn-QSY probe (red) and Hoechst (blue). Left panels are white light transmission images, second panels are Pyro-PtdEtn-QSY photosensitizer fluorescence images (Cy5 channel, 628/40 nm Ex, 692/40 nm Em, 0.5 s exposure time), and third panels show the fluorescence of the Hoechst nuclear stain (DAPI channel, 357/44 nm Ex, 447/60 nm Em, 0.01 s exposure time), with the right panels showing the overlaid images. Brightness and contrast settings of images are adjusted independently. Cell lines in panels: A–D (MDA-MB-231), E–H (MDA-MB-453), I–L (MCF-7), M–P (SKBR3), and Q–T (MCF-12A).

to the uptake (Figure S3d). The observed difference correlates with higher activity of PC–PLC in MDA-MB-231 cells compared to MCF7 cells (Figure S2).

The specificity of probe activation in cancer cells was confirmed using tricyclodecan-9-yl-xanthogenate (D609), a competitive inhibitor of PC–PLC. Treatment of cancer cells with 50 μg/mL of D609 has been demonstrated to induce a 3.5-fold decrease in PC–PLC activity within 1 h.[36] At high doses (>500 μM) and prolonged incubation times, the inhibitor induced apoptosis in breast cancer cells.[35,73] MDA-MB-231 cells were incubated with 5 or 50 μg/mL of D609 for 1 h prior to treatment with Pyro-PtdEtn-QSY probe for 1 h. Compared with the untreated control, D609 effectively inhibited the probe activation at 50 μg/mL concentration, and inhibition at the lower dose was still evident (Figure S4).

A series of fluorescent imaging experiments were performed to confirm cellular uptake of the probe, fluorophore activation, and probe localization within the cell structure (Figure 5). From the images, it is clear that the probe was successfully delivered and activated inside the cells. The activated probe was found in the cytoplasm of all cells, with higher probe accumulation observed in the organelles surrounding the

https://doi.org/10.1021/acs.bioconjchem.1c00295
Bioconjugate Chem. 2021, 32, 1852–1863

nucleus; this effect is especially profound in MCF-12A cells. It is clear that the probe does not penetrate through the nuclear membrane. Ultimately, understanding the probe distribution within the cells may play a key role in defining the mechanism of action of the probe as a therapeutic agent.

PDT experiments were conducted using the triple negative MDA-MB-231 cells. To define the initial set of concentrations and the drug–light interval (probe incubation time) for PDT experiments, we measured concentration-dependent probe activation (Figure 6) and the kinetics of probe accumulation and activation (Figure 7). MDA-MB-231 cells were incubated for 6 h with quenched Pyro-PtdEtn-QSY (Figure 6a) at various concentrations, and the fluorescence intensities of these samples were obtained using flow cytometry. Mean fluorescence intensity values from these experiments are plotted in Figure 6b.

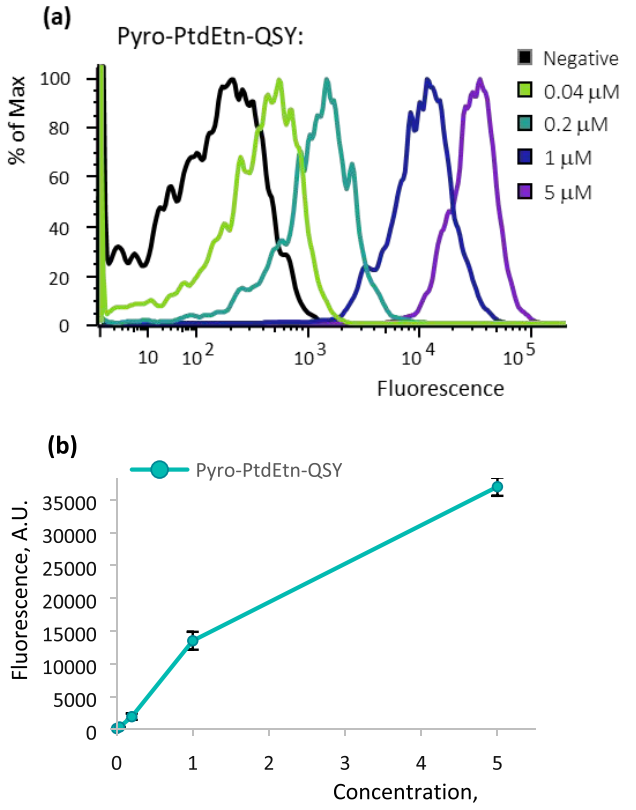

Figure 6. Dependence of MDA-MB-231 cell fluorescence on fluorophore concentration. The cells were incubated with Pyro-PtdEtn-QSY probe at different concentrations for 6 h before analysis by flow cytometry (a). The experiments were repeated three times and done in duplicate for each sample. Mean fluorescence intensity value and SD are plotted in (b) for each experimental point.

The Pyro-PtdEtn-QSY probe is thus readily absorbed by the cells, and a linear dependence between probe activation and concentration was observed at concentrations up to 1 μM. At higher concentration, the rate of probe activation was slightly decreased. To avoid probe saturation, a concentration lower than 1 μM, i.e., 0.66 μM, was chosen for the kinetics experiment.

The kinetics of the probe activation was investigated further. Cells were incubated with 0.66 μM Pyro-PtdEtn-QSY probe for various time intervals, and the fluorescence was measured (Figure 7a). A plateau in fluorescence was achieved after 8 h of incubation with the probe (Figure 7b). An incubation time of 12 h was chosen for PDT studies, as this time point provided high and stable activation levels.

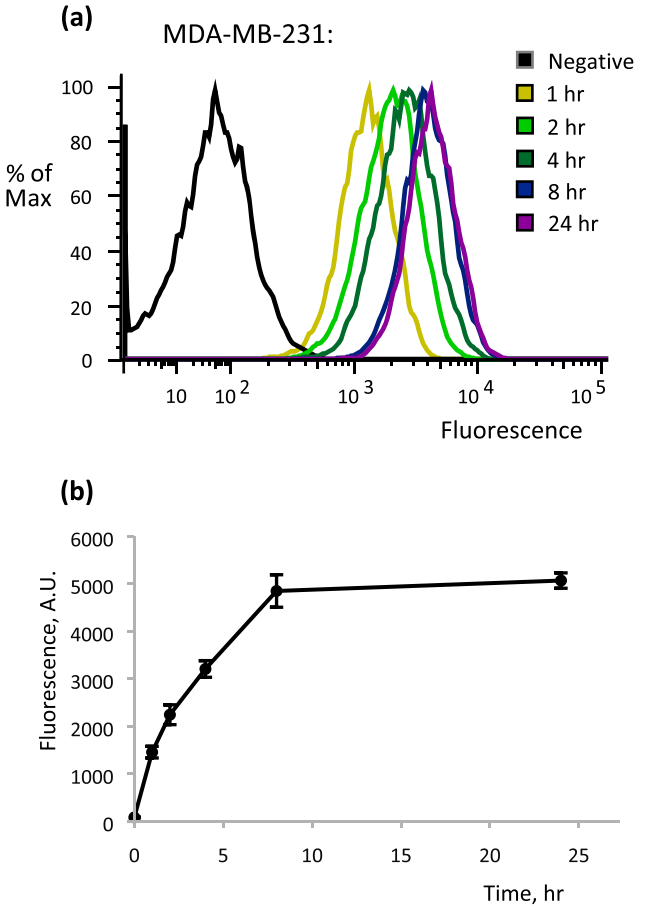

Figure 7. Pyro-PtdEtn-QSY probe activation over time. MDA-MB-231 cells were treated with 0.66 μM Pyro-PtdEtn-QSY probe in micelles for various incubation times, and the cell fluorescence was measured by flow cytometry (a). Each experimental point was tested in duplicate at least in three independent experiments. Mean values and standard deviation are calculated for each experimental point and plotted in (b).

PDT experiments were carried out using MDA-MB-231 cells to assess cell proliferation and the colony formation ability following 12 h incubation with the probe and illumination with 665 nm light.

MDA-MB-231 cell proliferation was studied using an MTT colorimetric assay following PDT. Pyro-PtdEtn-QSY probe concentrations of 0.66 μM and 6.6 μM were used with four different light doses of 0.5, 1, 2, and 4 J/cm^2 at 665 nm (Figure 8).

As evident from the experiment, 6.6 μM probe concentration is associated with stark dose-dependent cytotoxicity following PDT, leading to a 50-fold reduction in viability upon exposure to 4 J/cm^2 light dose. Incubation with the probe at 0.66 μM concentration reduced cell viability to 19.6 ± 7.5% of the baseline at the maximum light dose. Controls included cells that had no probe treatment and no light exposure, as well as cells incubated with either 0.66 μM or 6.6 μM probe but not subjected to light exposure. Results of control experiments were plotted as part of the concentration-dependent dark toxicity graph (Figure 9), along with three other concentrations—0.066 μM, 25 μM, and 66 μM, all in the absence of

https://doi.org/10.1021/acs.bioconjchem.1c00295
Bioconjugate Chem. 2021, 32, 1852−1863

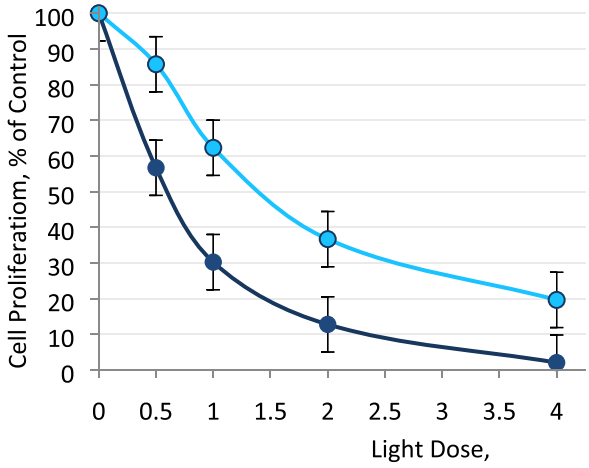

Figure 8. Relative proliferation (%) of the MDA-MB-231 tumor cells following PDT treatment as measured by an MTT assay. Cells were irradiated at 665 nm with a power density of 5 mW/cm^2 to doses of 0.5, 1.0, 2.0, and 4.0 J/cm^2 (for 100, 200, 400, and 800 s, respectively), and cell viability was measured by MTT assay. Light blue curve − 0.66 μM probe concentration; dark blue curve − 6.6 μM probe. Standard deviations from mean values are depicted by error bars (N = 3).

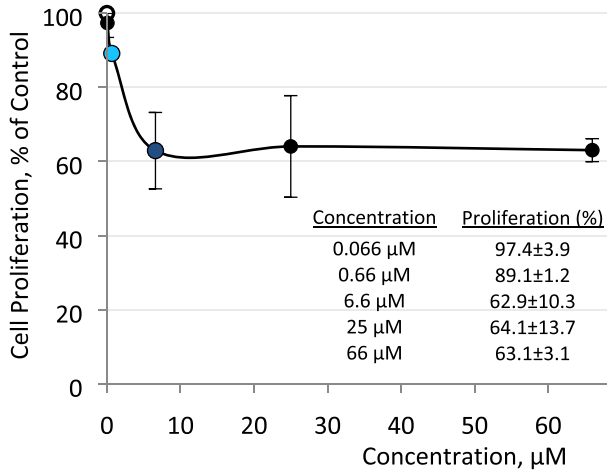

Figure 9. Cytotoxicity of Pyro-PtdEtn-QSY probe without light exposure. The dark toxicity experiment was performed by administering the probe at various concentrations to MDA-MB-231 cells without subjecting them to light exposure. Relative proliferation (%) is assessed by an MTT assay. The open circle (at 100% mark) represents the control cells, which were not treated with Pyro-PtdEtn-QSY probe, the light blue circle corresponds to the 0.66 μM probe concentration, and the dark blue circle to 6.6 μM. Mean values and standard deviation are indicated for each experimental point (N = 3).

665 nm light exposure. A control for light exposure in the absence of probe was conducted with cells lacking the probe treatment and illuminated with the highest light dose of 4 J/cm^2, resulting in 87.8% proliferation compared to untreated, unilluminated controls. The dark toxicity study revealed the probe toxicity at concentrations of 6.6 μM or greater. As a result, preference was given to the lower concentration of 0.66 μM.

While the MTT assay evaluates cell viability by assessing the mitochondrial reductive capacity, clonogenic assays assess the long-term proliferative potential of cells following PDT treatment. Clonogenic assays were conducted using 0.66 μM probe concentration and light doses of 0.5, 1, 2, and 4 J/cm^2 at 665 nm. Data were normalized to the plating efficiency of probe-free control cells, which did not undergo PDT treatment (Figure 10).

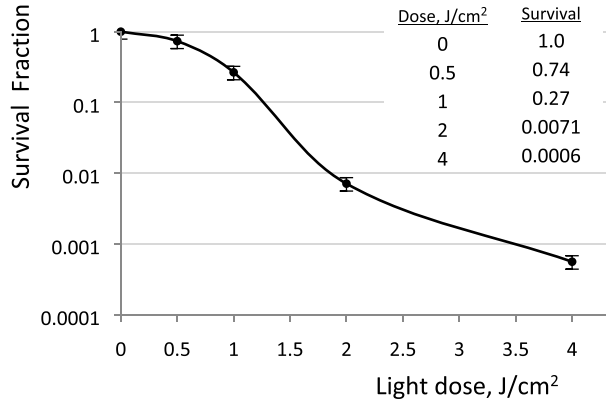

Figure 10. Normalized colony forming ability of MDA-MB-231 cells after treatment with PDT. Cells were incubated in the dark for 12 h with 0.66 μM probe prior to 665 nm light exposure using a 5 mW/cm^2 fluence rate and different exposure times. Error bars show the mean with SD for each point from three separate experiments.

The ability of cells to form colonies was dramatically impaired by PDT treatment, where the highest light dose is suppressing the colony formation ability by more than 1000-fold compared to the untreated control. Both the probe-free control cells treated with 4 J/cm^2 PDT and the probe-exposed cells receiving no PDT treatment showed a similar colony formation ability as the probe-free, PDT-free control cells (Table 1).

Table 1. Average Plating Efficiency of Colony Formation for Control Conditions

Probe-free, PDT-free control cells	40.8 ± 5.6%
Probe-free control cells with 4 J/cm^2 PDT	43.9 ± 7.6%
Probe-exposed cells with no PDT treatment	40.2 ± 2.8%

It is clear that treatment with the Pyro-PtdEtn-QSY probe followed by illumination for PDT significantly impairs the ability of MDA-MB-231 cells to multiply. The effect cannot be attributed to the 665 nm light exposure alone or dark toxicity from mere probe intake by cells without 665 nm light exposure. QSY21 is a FRET-based quencher. It has been shown that there is a strong correlation (R^2 = 0.98) between the fluorescent quenching of Pyro by FRET-based quenchers and singlet oxygen quenching.[74] Thus, the quencher deactivates the photosensitizer excited singlet state, drastically diminishing the PDT-induced toxicity of the quenched probe. As a result, the PC−PLC probe, Pyro-PtdEtn-QSY, does not have the properties of a photosensitizer prior to PC−PLC-induced cleavage. PDT could mediate unquenched (cleaved) probe self-bleaching due to the interaction of singlet oxygen with the Pyro moiety. However, it has been shown that the Pyro self-bleaching effect is minimal at the low light doses used for *in vitro* studies.[75]

The tissue penetration depth of the probe signal was also tested by diffuse optical imaging (DOT). In this case, micelles were loaded with unquenched Pyro-PtdCho and immersed into a scattering solution in an ∼1.6-cm-diameter cylindrical

https://doi.org/10.1021/acs.bioconjchem.1c00295
Bioconjugate Chem. 2021, 32, 1852−1863

container. The background scattering solution was designed to simulate human breast/breast-cancer tissue. The target (containing the probe solution) was placed at varying depths in a tank filled with an intralipid scattering solution. The tissue phantom surface was illuminated with a 670 nm excitation laser, and target fluorescence was detected using a 700 nm long-pass filter. The maximum detected fluorescence signal is plotted as a function of the probe immersion depth in Figure S5a. The control experiment, represented by the red line on the graph in Figure S5a, measured the maximum fluorescence background signal, originating from the target filled with HEPES buffer alone. The detected fluorescence levels generated by the Pyro-PtdCho probe were well above the background for depths of up to 3 cm. For the sample cell centered at 1.2 cm depth, the shape and the position of the target were successfully reconstructed based on the detected intensity on the tissue phantom surface (Figure S5b,c); these reconstructions used the NIRFAST DOT reconstruction suite.[76] The results provide feasibility for the fluorescence detection of activated Pyro-PtdEtn-QSY, intraoperatively.

In summary, we have shown that Pyro-PtdEtn-QSY can successfully penetrate cells, wherein it is activated and produces a detectable NIR fluorescence signal sufficient for imaging. All the breast cancer cell lines tested revealed increased probe activation levels compared to noncancerous control cells. The selectivity toward cancerous tissue is further enhanced by the inability of the unquenched probe, Pyro-PtdCho, to penetrate cells. PDT experiments showed that the Pyro-PtdEtn-QSY probe can be an effective agent against highly aggressive triple-negative MDA-MB-231 breast cancer cells. With both the absorbance and the fluorescence in the NIR range, optimal for tissue penetration, the probe could be employed in tumors located substantially below the surface. In the future, *in vivo* studies will be conducted to assess the ability of the probe in combination with PDT to detect and reduce the extent of cancer tumors in mouse models.

EXPERIMENTAL SECTION

Materials and General Methods. Pyropheophorbide *a* acid (Pyro) was purchased from Frontier Scientific, Newark, DE, USA. 1-Palmitoyl-2-hydroxy-*sn*-glycero-phosphoethanolamine (16:0 *Lyso*-phosphatidylethanolamine, LysoPtdEtn), 1-palmitoyl-2-hydroxy-*sn*-glycero-phosphocholine (16:0 *Lyso*-phosphatidylcholine, LysoPtdCho), 1,2-distearoyl-*sn*-glycero-3-ghosphoethanolamine-*N*-[methoxy(molyethylene glycol)-1000] ammonium salt (DSPE-PEG1000) in chloroform, 5 mg/mL, and 1,2-distearyl-*sn*-glycero-3-phosphoethanolamine-*N*-(TopFluor) AF488 in chloroform, 250 μg/mL (18:0 PE-TopFluor AF488, PtdEtn-AF488) were purchased from Avanti Polar Lipids, Inc., Alabaster, AL, USA. QSY21, succinimidyl ester (QSY-SE), was purchased from ThermoFisher Scientific, Grand Island, NY, USA.

Dry solvents were purchased from ACROS Organics. Regular solvents were purchased from Fisher Scientific. Other reagents/reactants were purchased from Sigma-Aldrich and used without further purification. Silica Diol (Premium Rf, 70A, 40−75 μm, product #62570−01) and Silica Diol thin layer chromatography plates (w/UV254, glass-backed, 200 μm, 10 × 20 cm 25/pk, product #2914136) were purchased from Sorbtech Chromatography, Norcross, GA, USA. All chemical reactions with QSY21 and/or Pyro were carried out in the dark under dry argon. MALDI-TOF mass-spectra were recorded on a Bruker Ultraflex III MALDI TOF/TOF (Bruker Daltonics, Billirica, MA, USA) using positive-mode ionization with a terthiophene (Ter; 2,2′:5′,2″-Terthiophene) matrix. Absorbance and fluorescence data were measured using a SpectraMax M5 fluorescent plate reader (Molecular Devices, San Jose, CA, USA) and an IVIS Spectrum In Vivo Imaging System (PerkinElmer, Hopkinton, MA, USA). Cell imaging experiments were perfomed using an EVOS Fluorescence Microscopy Imaging System (Thermo FisherScientific, Grand Island, NY, USA).

Synthesis of Molecular Probes and Lipid Nanoparticles. Pyro-PtdEtn-QSY and Pyro-PtdCho probes were synthesized and incorporated into lipid nanoparticles using established protocols[38] (Scheme S1) and[57−59] (Scheme S2), respectfully (SI).

Assembly and Characterization of Nanoparticles. Each fluorescent probe was dissolved in chloroform, and the absorption of the solution was measured at 410 nm. Using the extinction coefficient for Pyro (ε = 110,000 M^{-1} cm^{-1}),[27] the concentration of the probe solutions were determined. DSPE-PEG1000 was mixed with Pyro-PtdEtn-QSY or Pyro-PtdCho probe in dry chloroform at a molar ratio of 86.5:13.5 in a glass tube. In the experiments measuring nanoparticle binding and uptake, 3 mol % of phospholipids conjugated with Alexa Fluor 488 (PtdEtn-AF488) were included in a mixture containing quenched Pyro-PtdEtn-QSY. The chloroform was evaporated using argon flow, and the lipid film was dried under high vacuum for at least 3 h. The tube was flushed with argon, and the lipid film hydrated with hot (80 °C) degassed HBS buffer (10 mM Hepes, 140 mM NaCl) and intermittent vortexing. The resulting solution was cooled to room temperature and filtered through 0.2 μm filters (MILLEX-GV).[65] The micelle solution was kept in the dark at 4 °C.

The size distribution of the LNPs was measured by light-scattering photon correlation spectroscopy (Zetasizer NanoZS, Malvern Instruments, Malvern, UK) utilizing a 10 mW He−Ne laser operating at 633 nm and a detector angle of 90°. The data were modeled assuming spherical particles undergoing Brownian motion.[65]

The absorbance and fluorescence spectra of the micelles, carrying Pyro-PtdEtn-QSY and Pyro-PtdCho, were obtained in HEPES buffer (pH = 7.0) using a SpectraMax M5 fluorescent plate reader (Molecular Devices, San Jose, CA).

Cell Culture. Four breast cancer cell lines, MDA-MB-231, MDA-MB-453, MCF-7, and SKBR3 were obtained from the American Type Culture Collection (ATCC) and cultured in Dulbecco's modified Eagle's medium (DMEM) (Corning, 10-013-CM). The medium was supplemented with 10% fetal bovine serum (FBS) and 1% penicillin and streptomycin. The immortalized human mammary gland cell line MCF-12A was purchased from ATCC and cultured in DMEM F12 medium, supplemented with 5% horse serum, hydrocortisone (0.5 μg/mL), insulin (10 μg/mL), hEGF (20 ng/mL), and gentamicin (0.25 μg/mL)/amphotericin-B (10 μg/mL) (Gibco Laboratories, Grand Island, NY, USA). Cells were grown in 75 cm^2 flasks and passaged when 70−90% confluent. The cells were maintained in a humidified incubator at 37 °C and 5% CO_2 atmosphere.

Flow Cytometry Analysis of Probe Activation. Breast cancer cells were plated into 96-flat-well plates at 5 × 10^4 cells/well and grown overnight. The cytotoxic CD8 T cell line CER43 was utilized as a negative control.[65] Pyro-PtdEtn-QSY or Pyro-PtdCho probes were added at indicated concentrations and incubated for the chosen time interval. Cells

https://doi.org/10.1021/acs.bioconjchem.1c00295
Bioconjugate Chem. 2021, 32, 1852−1863

incubated with nanoparticles without fluorescent probes were utilized as negative controls. The wells were washed with DPBS buffer and incubated with DPBS containing 5 mM EDTA for 5 min at room temperature. Detached cells were washed with DPBS/1% BSA buffer and analyzed using a BD LSR II Flow Cytometer (BD Biosciences, San Jose, CA). Pyrofluorescence was measured with 633 nm laser and 670/30 bandpass filter.

Double-labeled nanoparticles containing both the quenched Pyro-PtdEtn-QSY and the PtdEtn-AF488 lipid were used to simultaneously measure cellular nanoparticle uptake (AF488 fluorescence) and probe activation (Pyro fluorescence). AF488 fluorescence was measured using a 488 nm laser and 530/30 bandpass filter. Each time when AF488 cellular fluorescence was measured, Alexa Fluor 488 Quantum MESF microspheres (Bangs laboratories Inc., Fishers, IN, USA) were used. Microsphere populations are surface-labeled with increasing amounts of the fluorochrome calibrated in MESF units. The microbeads served both as a quality control and as an AF488 intensity calibrator. Probe uptake was calculated using the AF488 fluorescence intensity of nanoparticle-treated cells with values expressed as MESF. Pyro-PtdEtn-QSY probe activation measured as cell fluorescence using the Pyro channel was normalized relative to probe uptake employing the equation

$$(\mathrm{MFI(Pyro)} - \mathrm{MFI(negative)})/(\mathrm{MESF(AF488)} - \mathrm{MESF(negative)})$$

where MFI(Pyro) is cellular fluorescence of activated Pyro-PtdEtn-QSY probe, MFI(negative) is cell autofluorescence in the Pyro channel, MESF(AF488) is the number of AF488 fluorophores per cell, and MESF(negative) is the cell autofluorescence in the AF488 channel expressed in MESF units.

The effects of the PC−PLC inhibitor D609 on Pyro-PtdEtn-QSY probe activation were monitored. D609 was dissolved in dry DMSO at 25 mg/mL and stored desiccated at −80 °C. Cells were plated in a 96-well plate. After incubation overnight, cells were treated with 5 or 50 μg/mL D609 for 1 h. Micelles bearing the quenched Pyro-PtdEtn-QSY and the PtdEtn-AF488 lipids were added to the wells to a final concentration of 1 μM, and incubation continued for one more hour. The cells were collected, washed, and analyzed by flow cytometry, and probe activation was normalized relative to probe uptake as described above. D609 inhibition of the probe activation was calculated relative to the untreated control and expressed as a percentage.

Amplex Red Assay of PC−PLC Activity in Whole Cell Lysates. Breast cancer cell line were grown until confluent. Cell lysis was performed using a lysis buffer (12 mM Tris-HCl, pH 7.2; 140 mM NaCl; 0.75 mM EDTA, 0.25% Triton X-100) on ice for 20 min in the presence of protease and phosphatase inhibitors (5 μg/mL aprotinin, 5 μg/mL pepstatin A, 5 μg/mL leupeptin; 100 μM sodium orthovanadate, and 100 μM PMSF). The lysates were spun at 13,000 rpm, and supernatants were collected. Protein concentration was measured using a BCA Protein Assay (Pierce). When needed, the supernatants were diluted in order to have the same concentration of protein. PC−PLC activity was measured in supernatant using an Amplex Red Phosphatidylcholine-Specific Phospholipase C Assay Kit (Molecular Probe, Inc., Eugene, OR, USA).[29] Briefly, the supernatants were mixed with equal amounts of working solution containing 2 U/mL horseradish peroxidase (HRP), 8 U/mL alkaline phosphatase, 0.2 U/mL choline oxidase, 1 mM phosphatidylcholine, and 0.4 mM Amplex Red reagent in 1× Reaction Buffer (50 mM Tris-HCl, pH 7.4, 0.14 M NaCl, 10 mM dimethylglutarate, 2 mM $CaCl_2$). The experiment was performed in triplicate. Phosphocholine released from phosphatidylcholine by PC−PLC is converted to choline by alkaline phosphatase, which is further oxidized to form H_2O_2. In the presence of HRP, H_2O_2 reacts with Amplex Red to generate the fluorophore, resorufin, which was detected using λ_{ex} = 560 nm and λ_{em} = 590 nm on the SpectraMax M5 plate reader.

Analysis of Probe Activation by Microscopy. For microscopy experiments, cells were grown in phenol-red free DMEM media with 10% FBS. Cells were treated with a Pyro-PtdEtn-QSY probe solution in HEPES buffer, resulting in a 6.6 μM Pyro-PtdEtn-QSY concentration. After 30 min incubation in a 5% CO_2 environment at 37 °C, the media was replaced with the original media without the probe, and cells were imaged. Nuclei were stained with 1.5 μM Hoechst solution 3 h prior to microscopy. Images of different cell lines were obtained using an EVOS Fluorescence Microscopy Imaging System equipped with a Cy5 filter cube set and DAPI channel cube set.

MTT Viability Assay. MDA-MB-231 cells were seeded in black-walled 96-well plates (PerkinElmer, 6005182) at 1.5 × 10^4 cells/well in 150 μL of media and incubated for 24 h. The cells were washed with 200 μL of HBSS solution (Gibco, 14175−079) and bathed in 100 μL of freshly prepared media containing either 0.66 μM or 6.6 μM probe; controls received fresh media without the probe. All samples were tested in triplicate. After 12 h of incubation, the media was removed, the wells were washed with 200 μL of HBSS, and the wells filled with 50 μL of media containing 5% FBS. The plates were irradiated at 665 nm with a power density of 5 mW/cm^2 to doses of 0.5, 1.0, 2.0, and 4.0 J/cm^2 (for 100, 200, 400, and 800 s, respectively). Illumination was provided by a B&W Tek Inc. diode laser and delivered through microlens-tipped fibers. Light was measured via a Labmaster power meter (Coherent). After irradiation, 50 μL of media containing 15% FBS was added to each well, bringing the overall FBS concentration to 10% for subsequent incubation. Plates were incubated in the dark for 24 h. Cell viability was measured by the MTT colorimetric assay (Roche, 11465007001) and recorded as the percentage of live cells in the illuminated samples compared to the percentage of live cells in the control with no light exposure for each concentration.

Dark toxicity experiments were carried using the same protocol, except no illumination was involved.

Clonogenic Assay for Colony Formation. MDA-MB-231 cells were seeded into two 75 cm^2 flasks at 1.5 × 10^6 cells per flask. Cells were allowed to grow for 60 h, and then the flasks were rinsed with 10 mL of HBSS. 10 mL of 0.66 μM probe solution in low serum media (5% FBS) was added to the treatment flask, and 10 mL of low serum media was added to the control flask. After 12 h of incubation, both flasks were rinsed with HBSS, and 10 mL of low serum media was added to each flask, followed by 1 h incubation. The cells were trypsinized, counted, and resuspended in low serum media as 2 × 10^5 cells/mL. 2 mL aliquots of probe-exposed cells were transferred to 60 × 15 mm Petri dishes, and treated with 665 nm PDT at 5 mW/cm^2 to a total fluence of 0.5, 1, 2, and 4 J/cm^2 (100, 200, 400, and 800 s, respectively). A 2 mL aliquot of the probe-free control cells was treated to the highest dose of 4

https://doi.org/10.1021/acs.bioconjchem.1c00295
Bioconjugate Chem. 2021, 32, 1852−1863

J/cm^2. Irradiated cells were then plated in triplicates in 100 × 20 mm^2 tissue culture dishes filled with 10 mL of regular growth media (10% FBS in DMEM) at 10^2, 10^3, 10^4, and 10^5 cells/plate. In addition, both the probe-exposed cells and probe-free control cells with no irradiation were plated at 10^2 cells/well. Dishes with cells were placed in a 37 °C incubator (5% CO_2) for 12 days. Following incubation, the media was drained, and the dishes were allowed to dry and stained with 0.25% Methylene Blue solution in 95% ethanol. Colonies were then counted. This experiment was repeated three times. The plating efficiency was determined as [(#colonies counted/# cells plated) × 100%], and survival fractions were calculated by normalizing to the plating efficiency under control conditions. Averaged results were plotted in a log scale as a function of the light dose.

Fluorescence Diffuse Optical Tomography. A continuous-wave (CW) 670 nm diode laser (Thorlabs, HL6756MG) was collimated, passed through a laser line filter (Thorlabs, FL670−10), and then directed to a galvanometer scanner (Thorlabs, GVS012). The source laser light was scanned over a 9 × 9 grid of source locations spanning a total area of 12 cm × 12 cm on the side of an imaging tank; a similar setup is employed and described in previous work.[77] An imaging camera (Hamamatsu, ORCA-Flash 4.0 C11440) was placed beside the galvanometer scanner to capture fluorescence emission in the reflection geometry; the emitted fluorescence light was filtered by a 700 nm long-pass filter (Edmund Optics, 64703). For each point on the scanned grid, the image was captured with a 1 s exposure time. A cylindrical target, approximately 1.6 cm in diameter and height,[78] was filled with a solution of 8 μM Pyro-PtdCho micelles in HEPES buffer. The cylindrical target was placed inside a tank filled with Intralipid solution that mimicked the scattering properties of breast tissue (reduced scattering coefficient $\mu_s' = 8$ cm^{-1} at 785 nm). The target was immersed in the tank and positioned approximately in the center of the camera's field of view. The target depth from the illumination surface was varied from 1.2 to 3.7 cm, as measured to the center of the target, in 0.5 cm increments. A measurement was taken using the pure HEPES buffer solution, i.e., without the fluorophore, in the target to provide background data and to facilitate a "difference" reconstruction algorithm. The reconstruction was performed using a fluorescence finite difference method available in the NIRFAST software suite.[76]

■ ASSOCIATED CONTENT

Supporting Information

The Supporting Information is available free of charge at https://pubs.acs.org/doi/10.1021/acs.bioconjchem.1c00295.

Syntheses of the fluoroprobes; fluorescence intensity from various cell types measured by flow cytometry; nanoparticle size distribution; absorbance and fluorescence of the fluoroprobes in micelles; measurement of PC−PLC activity in different cell lines; evaluation of probe uptake by flow cytometry; fluorescence diffuse optical tomography results (PDF)

■ AUTHOR INFORMATION

Corresponding Author

Anatoliy V. Popov − *Department of Radiology, Perelman School of Medicine, University of Pennsylvania, Philadelphia, Pennsylvania 19104, United States;* orcid.org/0000-0002-4678-6307; Email: avpopov@pennmedicine.upenn.edu

Authors

Natalia I. Rubtsova − *Department of Radiology, Perelman School of Medicine, University of Pennsylvania, Philadelphia, Pennsylvania 19104, United States*

Michael C. Hart − *Department of Radiology, Perelman School of Medicine, University of Pennsylvania, Philadelphia, Pennsylvania 19104, United States*

Alejandro D. Arroyo − *Department of Radiology, Perelman School of Medicine, University of Pennsylvania, Philadelphia, Pennsylvania 19104, United States;* Present Address: Memorial Sloan Kettering Cancer Center, 1275 York Avenue, New York, NY 10065

Sofya A. Osharovich − *Department of Radiology, Perelman School of Medicine, University of Pennsylvania, Philadelphia, Pennsylvania 19104, United States*

Benjamin K. Liebov − *Department of Radiology, Perelman School of Medicine, University of Pennsylvania, Philadelphia, Pennsylvania 19104, United States;* Present Address: Adesis, Inc., 27 McCullough Drive, New Castle, DE 19720, USA

Joann Miller − *Department of Radiation Oncology, Perelman School of Medicine, University of Pennsylvania, Philadelphia, Pennsylvania 19104, United States*

Min Yuan − *Department of Radiation Oncology, Perelman School of Medicine, University of Pennsylvania, Philadelphia, Pennsylvania 19104, United States*

Jeffrey M. Cochran − *Department of Physics and Astronomy, University of Pennsylvania, Philadelphia, Pennsylvania 19104, United States*

Sanghoon Chong − *Department of Physics and Astronomy, University of Pennsylvania, Philadelphia, Pennsylvania 19104, United States*

Arjun G. Yodh − *Department of Physics and Astronomy, University of Pennsylvania, Philadelphia, Pennsylvania 19104, United States;* orcid.org/0000-0003-4744-2706

Theresa M. Busch − *Department of Radiation Oncology, Perelman School of Medicine, University of Pennsylvania, Philadelphia, Pennsylvania 19104, United States*

E. James Delikatny − *Department of Radiology, Perelman School of Medicine, University of Pennsylvania, Philadelphia, Pennsylvania 19104, United States*

Nadia Anikeeva − *Department of Microbiology and Immunology, Thomas Jefferson University, Philadelphia, Pennsylvania 19107, United States*

Complete contact information is available at: https://pubs.acs.org/10.1021/acs.bioconjchem.1c00295

Notes

The authors declare no competing financial interest.

■ ACKNOWLEDGMENTS

This work was supported by the National Cancer Institute (NCI) grant, R01-CA201328. BKL's, NIR's, and AVP's work was partially supported by R01-NS100892. NIR's and AVP's work was partially supported by the University of Pennsylvania Ovarian Cancer TCE Research Award. EJD's and SAO's work was partially supported by R01-CA226412. ADA's work was partially supported by F31-CA206453. Imaging was performed at the University of Pennsylvania Small Animal Imaging Facility (SAIF). Microscopy was performed at the University

of Pennsylvania Cell and Developmental Biology (CDB) Microscopy Core.

■ ABBREVIATIONS

AF488, Alexa Fluor 488 carboxylic acid, 2-(6-amino-3-iminio-4,5-disulfonato-3*H*-xanthen-9-yl)-(4 and 5)-carboxybenzoate dilithium salt; Amplex Red, 1-(3,7-dihydroxy-10*H*-phenoxazin-10-yl)ethan-1-one; ATCC, American Type Culture Collection; BCA, bicinchoninic acid; BHQ-3 carboxylic acid, black hole quencher-3, 3-diethylamino-5-phenylphenazium-7-diazobenzene-4″-(*N*-methyl)-*N*-butyric acid; Cho, choline; CW, continuous-wave; D609, tricyclodecan-9-yl-xanthogenate; DMEM, Dulbecco's modified Eagle's medium; DMSO, dimethyl sulfoxide; DOT, diffuse optical tomography; DSPE-PEG(1000), 1,2-distearyl-*sn*-glycero-3-phosphoethanolamine-*N*-[methoxy(polyethylene glycol)-1000] (ammonium salt; DU145, a human prostate cancer cell line. DU stands for Duke University; EGFR, epidermal growth factor receptor; Etn, ethanolamine; FBS, fetal bovine serum; FRET, Förster resonance energy transfer; HBSS, Hank's Balanced Salt Solution; HEPES, 2-(4-(2-hydroxyethyl)piperazin-1-yl)-ethane-1-sulfonic acid; HER2, human epidermal growth factor receptor 2; HRP, horseradish peroxidase; LNPs, lipid-based nanoparticles; MALDI-TOF, Matrix Assisted Laser Desorption/Ionization Time-of-Flight Mass Spectrometry; MCF-7, a human breast cancer cell line. MCF stands for "Michigan Cancer Foundation"; MCF-12A, nontumorigenic mammary epithelial cells; MDA-MB-231, a human triple-negative breast cancer cell line. MDA stands for "M.D. Anderson" and MB stands for "Metastasis Breast cancer"; MDA-MB-453, a human triple-negative breast cancer cell line.; MESF, Molecules of Equivalent Soluble Fluorochrome; Methylene Blue, *N*-(7-(dimethylamino)-3*H*-phenothiazin-3-ylidene)-*N*-methylmethanaminium chloride; MTT, 3-(4,5-dimethylthiazol-2-yl)-2,5-diphenyl-2*H*-tetrazol-3-ium bromide; NIR, near-infrared; NIRF, near-infrared fluorophore; PC, phosphocholine; PC−PLC, phosphatidylcholine-specific phospholipase C; PDT, photodynamic therapy; PBMC, peripheral blood mononuclear cells; PMSF, phenylmethylsulfonyl fluoride; PtdCho, phosphatidylcholine; PtdEtn, phosphatidylethanolamine; PtdEtn-AF488, 1,2-distearyl-*sn*-glycero-3-phosphoethanolamine-*N*-(TopFluor) AF 488 ammonium salt; Pyro, pyropheophorbide *a*; Pyro-PtdCho, 1-palmitoyl-2-pyropheophorbide *a*-*sn*-glycero-3-phosphocholine; Pyro-PtdEtn-BHQ, 1-palmitoyl-2-pyropheophorbide *a*-*sn*-glycero-3-phosphoethanolamide of BHQ-3 carboxylic acid; Pyro-PtdEtn-QSY, 1-palmitoyl-2-pyropheophorbide *a*-*sn*-glycero-3-phosphoethanolamide of QSY21 carboxylic acid; QSY21 carboxylic acid, (*E*)-1-(9-(2-((4-carboxypiperidin-1-yl)sulfonyl)phenyl)-6-(indolin-1-yl)-3*H*-xanthen-3-ylidene)indolin-1-ium chloride; Resorufin, 7-hydroxy-3*H*-phenoxazin-3-one; SKBR3, a human breast cancer cell line. SK stands for Sloan-Kettering; BR, BReast cancer; Tris, tris(hydroxymethyl)aminomethane

■ REFERENCES

(1) Carey, L., Winer, E., Viale, G., Cameron, D., and Gianni, L. (2010) Triple-negative breast cancer: disease entity or title of convenience? *Nat. Rev. Clin. Oncol. 7* (12), 683−92.

(2) Won, K.-A., and Spruck, C. (2020) Triple-negative breast cancer therapy: current and future perspectives (review). *Int. J. Oncol. 57* (6), 1245−1261.

(3) Verhille, M., Couleaud, P., Vanderesse, R., Brault, D., Barberi-Heyob, M., and Frochot, C. (2010) Modulation of photosensitization processes for an improved targeted photodynamic therapy. *Curr. Med. Chem. 17* (32), 3925−3943.

(4) Ridgway, N. D. (2013) The role of phosphatidylcholine and choline metabolites to cell proliferation and survival. *Crit. Rev. Biochem. Mol. Biol. 48* (1), 20−38.

(5) Glunde, K., Bhujwalla, Z. M., and Ronen, S. M. (2011) Choline metabolism in malignant transformation. *Nat. Rev. Cancer 11* (12), 835−848.

(6) Negendank, W. (1992) Studies of human tumors by MRS: a review. *NMR Biomed. 5* (5), 303−24.

(7) Ackerstaff, E., Pflug, B. R., Nelson, J. B., and Bhujwalla, Z. M. (2001) Detection of increased choline compounds with proton nuclear magnetic resonance spectroscopy subsequent to malignant transformation of human prostatic epithelial cells. *Cancer Res. 61* (9), 3599−3603.

(8) Kurhanewicz, J., Vigneron, D. B., and Nelson, S. J. (2000) Three-dimensional magnetic resonance spectroscopic imaging of brain and prostate cancer. *Neoplasia 2* (1−2), 166−89.

(9) Swindle, P., McCredie, S., Russell, P., Himmelreich, U., Khadra, M., Lean, C., and Mountford, C. (2003) Pathologic characterization of human prostate tissue with proton MR spectroscopy. *Radiology 228* (1), 144−51.

(10) Milkevitch, M., Shim, H., Pilatus, U., Pickup, S., Wehrle, J. P., Samid, D., Poptani, H., Glickson, J. D., and Delikatny, E. J. (2005) Increases in NMR-visible lipid and glycerophosphocholine during phenylbutyrate-induced apoptosis in human prostate cancer cells. *Biochim. Biophys. Acta, Mol. Cell Biol. Lipids 1734* (1), 1−12.

(11) Podo, F. (1999) Tumour phospholipid metabolism. *NMR Biomed. 12* (7), 413−439.

(12) Bhakoo, K. K., Williams, S. R., Florian, C. L., Land, H., and Noble, M. D. (1996) Immortalization and transformation are associated with specific alterations in choline metabolism. *Cancer Res. 56* (20), 4630−4635.

(13) Li, X., Lu, Y., Pirzkall, A., McKnight, T., and Nelson, S. J. (2002) Analysis of the spatial characteristics of metabolic abnormalities in newly diagnosed glioma patients. *J. Magn Reson Imaging 16* (3), 229−37.

(14) Maris, J. M., Evans, A. E., McLaughlin, A. C., D'Angio, G. J., Bolinger, L., Manos, H., and Chance, B. (1985) 31P nuclear magnetic resonance spectroscopic investigation of human neuroblastoma in situ. *N. Engl. J. Med. 312* (23), 1500−5.

(15) Bagnoli, M., Granata, A., Nicoletti, R., Mezzanzanica, D., Krishnamachary, B., Bhujwalla, Z. M., Canese, R., Podo, F., Iorio, E., and Canevari, S. (2016) Choline Metabolism Alteration: A Focus on Ovarian Cancer. *Front. Oncol. 6*, 153.

(16) Iorio, E., Mezzanzanica, D., Alberti, P., Spadaro, F., Ramoni, C., D'Ascenzo, S., Millimaggi, D., Pavan, A., Dolo, V., Canevari, S., et al. (2005) Alterations of choline phospholipid metabolism in ovarian tumor progression. *Cancer Res. 65* (20), 9369−9376.

(17) Iorio, E., Ricci, A., Bagnoli, M., Pisanu, M. E., Castellano, G., Di Vito, M., Venturini, E., Glunde, K., Bhujwalla, Z. M., Mezzanzanica, D., et al. (2010) Activation of Phosphatidylcholine Cycle Enzymes in Human Epithelial Ovarian Cancer Cells. *Cancer Res. 70* (5), 2126−2135.

(18) Maurmann, L., Belkacemi, L., Adams, N. R., Majmudar, P. M., Moghaddas, S., and Bose, R. N. (2015) A novel cisplatin mediated apoptosis pathway is associated with acid sphingomyelinase and FAS proapoptotic protein activation in ovarian cancer. *Apoptosis 20* (7), 960−974.

(19) Paris, L., Podo, F., Abalsamo, L., Pisanu, M. E., Ricci, A., Cecchetti, S., Altabella, L., Ramoni, C., Iorio, E., Canese, R., et al. (2017) Phosphatidylcholine-specific phospholipase C inhibition reduces HER2-overexpression, cell proliferation and in vivo tumor growth in a highly tumorigenic ovarian cancer model. *Oncotarget 8* (33), 55022−55038.

(20) Podo, F., Paris, L., Cecchetti, S., Spadaro, F., Abalsamo, L., Ramoni, C., Ricci, A., Pisanu, M. E., Canese, R., Iorio, E., et al. (2016) Activation of Phosphatidylcholine-Specific Phospholipase C in Breast

https://doi.org/10.1021/acs.bioconjchem.1c00295
Bioconjugate Chem. 2021, 32, 1852−1863

and Ovarian Cancer: Impact on MRS-Detected Choline Metabolic Profile and Perspectives for Targeted Therapy. *Front. Oncol. 6*, 171.
(21) Spadaro, F., Ramoni, C., Mezzanzanica, D., Miotti, S., Alberti, P., Cecchetti, S., Iorio, E., Dolo, V., Canevari, S., and Podo, F. (2008) Phosphatidylcholine-Specific Phospholipase C Activation in Epithelial Ovarian Cancer Cells. *Cancer Res. 68* (16), 6541−6549.
(22) Jacobs, M. A., Barker, P. B., Bottomley, P. A., Bhujwalla, Z., and Bluemke, D. A. (2004) Proton magnetic resonance spectroscopic imaging of human breast cancer: a preliminary study. *J. Magn Reson Imaging 19* (1), 68−75.
(23) Singer, S., Souza, K., and Thilly, W. G. (1995) Pyruvate utilization, phosphocholine and adenosine triphosphate (ATP) are markers of human breast tumor progression: a 31P- and 13C-nuclear magnetic resonance (NMR) spectroscopy study. *Cancer Res. 55* (22), 5140−5.
(24) Katz-Brull, R., and Degani, H. (1996) Kinetics of choline transport and phosphorylation in human breast cancer cells; NMR application of the zero trans method. *Anticancer Res. 16* (3B), 1375−1379.
(25) Gribbestad, I. S., Sitter, B., Lundgren, S., Krane, J., and Axelson, D. (1999) Metabolite composition in breast tumors examined by proton nuclear magnetic resonance spectroscopy. *Anticancer Res. 19* (3A), 1737−1746.
(26) Glunde, K., Jie, C., and Bhujwalla, Z. M. (2004) Molecular Causes of the Aberrant Choline Phospholipid Metabolism in Breast Cancer. *Cancer Res. 64* (12), 4270−4276.
(27) Popov, A. V., Mawn, T. M., Kim, S., Zheng, G., and Delikatny, E. J. (2010) Design and Synthesis of Phospholipase C and A2-Activatable Near-Infrared Fluorescent Smart Probes. *Bioconjugate Chem. 21* (10), 1724−1727.
(28) Mawn, T. M., Popov, A. V., and Delikatny, E. J. (2012) A quantitative continuous enzyme assay of intramolecularly quenched fluorogenic phospholipase substrates for molecular imaging. *Anal. Biochem. 422* (2), 96−102.
(29) Mawn, T. M., Popov, A. V., Beardsley, N. J., Stefflova, K., Milkevitch, M., Zheng, G., and Delikatny, E. J. (2011) In Vivo Detection of Phospholipase C by Enzyme-Activated Near-Infrared Probes. *Bioconjugate Chem. 22* (12), 2434−2443.
(30) Kumar, M., Arlauckas, S. P., Saksena, S., Verma, G., Ittyerah, R., Pickup, S., Popov, A. V., Delikatny, E. J., and Poptani, H. (2015) Magnetic Resonance Spectroscopy for Detection of Choline Kinase Inhibition in the Treatment of Brain Tumors. *Mol. Cancer Ther. 14* (4), 899−908.
(31) Chiorazzo, M. G., Bloch, N. B., Popov, A. V., and Delikatny, E. J. (2015) Synthesis and Evaluation of Cytosolic Phospholipase A2 Activatable Fluorophores for Cancer Imaging. *Bioconjugate Chem. 26* (12), 2360−2370.
(32) Arlauckas, S. P., Popov, A. V., and Delikatny, E. J. (2016) Choline kinase alpha-Putting the ChoK-hold on tumor metabolism. *Prog. Lipid Res. 63*, 28−40.
(33) Arlauckas, S. P., Popov, A. V., and Delikatny, E. J. (2014) Direct Inhibition of Choline Kinase by a Near-Infrared Fluorescent Carbocyanine. *Mol. Cancer Ther. 13* (9), 2149−2158.
(34) Chiorazzo, M. G., Tunset, H. M., Popov, A. V., Johansen, B., Moestue, S., and Delikatny, E. J. (2019) Detection and Differentiation of Breast Cancer Sub-Types using a cPLA2α Activatable Fluorophore. *Sci. Rep. 9* (1), 1−11.
(35) Abalsamo, L., Spadaro, F., Bozzuto, G., Paris, L., Cecchetti, S., Lugini, L., Iorio, E., Molinari, A., Ramoni, C., and Podo, F. (2012) Inhibition of phosphatidylcholine-specific phospholipase C results in loss of mesenchymal traits in metastatic breast cancer cells. *Breast Cancer Res. 14*, R50.
(36) Paris, L., Cecchetti, S., Spadaro, F., Abalsamo, L., Lugini, L., Pisanu, M. E., Iorio, E., Natali, P. G., Ramoni, C., and Podo, F. (2010) Inhibition of phosphatidylcholine-specific phospholipase C down-regulates HER2 overexpression on plasma membrane of breast cancer cells. *Breast Cancer Res. 12* (3), R27.
(37) Cecchetti, S., Bortolomai, I., Ferri, R., Mercurio, L., Canevari, S., Podo, F., Miotti, S., and Iorio, E. (2015) Inhibition of phosphatidylcholine-specific phospholipase C interferes with proliferation and survival of tumor initiating cells in squamous cell carcinoma. *PLoS One 10* (9), No. e0136120.
(38) Liebov, B. K., Arroyo, A. D., Rubtsova, N. I., Osharovich, S. A., Delikatny, E. J., and Popov, A. V. (2018) Nonprotecting Group Synthesis of a Phospholipase C Activatable Probe with an Azo-Free Quencher. *ACS Omega 3* (6), 6867−6873.
(39) Liu, H., Zhao, M., Wang, J., Pang, M., Wu, Z., Zhao, L., Yin, Z., and Hong, Z. (2016) Photodynamic therapy of tumors with pyropheophorbide-a-loaded polyethylene glycol-poly(lactic-co-glycolic acid) nanoparticles. *Int. J. Nanomed. 11*, 4905−4918.
(40) Cheng, J., Tan, G., Li, W., Li, J., Wang, Z., and Jin, Y. (2016) Preparation, characterization and in vitro photodynamic therapy of a pyropheophorbide-a-conjugated Fe3O4 multifunctional magneto-fluorescence photosensitizer. *RSC Adv. 6* (44), 37610−37620.
(41) Zhou, A., Wei, Y., Wu, B., Chen, Q., and Xing, D. (2012) Pyropheophorbide A and c(RGDyK) Comodified Chitosan-Wrapped Upconversion Nanoparticle for Targeted Near-Infrared Photodynamic Therapy. *Mol. Pharmaceutics 9* (6), 1580−1589.
(42) Guo, Z., Park, S., Yoon, J., and Shin, I. (2014) Recent progress in the development of near-infrared fluorescent probes for bioimaging applications. *Chem. Soc. Rev. 43* (1), 16−29.
(43) Ballerstadt, R., Gowda, A., and McNichols, R. (2004) Fluorescence Resonance Energy Transfer-Based Near-Infrared Fluorescence Sensor for Glucose Monitoring. *Diabetes Technol. Ther. 6* (2), 191−200.
(44) de la Zerda, A., Bodapati, S., Teed, R., May, S. Y., Tabakman, S. M., Liu, Z., Khuri-Yakub, B. T., Chen, X., Dai, H., and Gambhir, S. S. (2012) Family of Enhanced Photoacoustic Imaging Agents for High-Sensitivity and Multiplexing Studies in Living Mice. *ACS Nano 6* (6), 4694−4701.
(45) Jolivel, V., Arthaud, S., Botia, B., Portal, C., Delest, B., Clave, G., Leprince, J., Romieu, A., Renard, P.-Y., Touzani, O., et al. (2014) Biochemical Characterization of a Caspase-3 Far-red Fluorescent Probe for Non-invasive Optical Imaging of Neuronal Apoptosis. *J. Mol. Neurosci. 54* (3), 451−462.
(46) Kokko, T., Kokko, L., Loevgren, T., and Soukka, T. (2007) Homogeneous Noncompetitive Immunoassay for 17β-Estradiol Based on Fluorescence Resonance Energy Transfer. *Anal. Chem. (Washington, DC, U. S.) 79* (15), 5935−5940.
(47) Le Reste, L., Hohlbein, J., Gryte, K., and Kapanidis, A. N. (2012) Characterization of Dark Quencher Chromophores as Nonfluorescent Acceptors for Single-Molecule FRET. *Biophys. J. 102* (11), 2658−2668.
(48) Li, X., Mu, J., Liu, F., Tan, E. W. P., Khezri, B., Webster, R. D., Yeow, E. K. L., and Xing, B. (2015) Human Transport Protein Carrier for Controlled Photoactivation of Antitumor Prodrug and Real-Time Intracellular Tumor Imaging. *Bioconjugate Chem. 26* (5), 955−961.
(49) Madiyar, F. R., Bhana, S., Swisher, L. Z., Culbertson, C. T., Huang, X., and Li, J. (2015) Integration of a nanostructured dielectrophoretic device and a surface-enhanced Raman probe for highly sensitive rapid bacteria detection. *Nanoscale 7* (8), 3726−3736.
(50) Ofori, L. O., Withana, N. P., Prestwood, T. R., Verdoes, M., Brady, J. J., Winslow, M. M., Sorger, J., and Bogyo, M. (2015) Design of Protease Activated Optical Contrast Agents That Exploit a Latent Lysosomotropic Effect for Use in Fluorescence-Guided Surgery. *ACS Chem. Biol. 10* (9), 1977−1988.
(51) Ogawa, M., Kosaka, N., Choyke, P. L., and Kobayashi, H. (2009) Tumor-Specific Detection of an Optically Targeted Antibody Combined with a Quencher-Conjugated Neutravidin"“" "Quencher-Chaser"“: A Dual"“" "Quench and Chase"“" Strategy to Improve Target to Nontarget Ratios for Molecular Imaging of Cancer. *Bioconjugate Chem. 20* (1), 147−154.
(52) Sun, X., Zhang, A., Baker, B., Sun, L., Howard, A., Buswell, J., Maurel, D., Masharina, A., Johnsson, K., Noren, C. J., et al. (2011) Development of SNAP-Tag Fluorogenic Probes for Wash-Free Fluorescence Imaging. *ChemBioChem 12* (14), 2217−2226.
(53) Verdoes, M., Oresic Bender, K., Segal, E., van der Linden, W. A., Syed, S., Withana, N. P., Sanman, L. E., and Bogyo, M. (2013)

https://doi.org/10.1021/acs.bioconjchem.1c00295
Bioconjugate Chem. 2021, 32, 1852−1863

Improved Quenched Fluorescent Probe for Imaging of Cysteine Cathepsin Activity. *J. Am. Chem. Soc. 135* (39), 14726−14730.
(54) Xing, B., Khanamiryan, A., and Rao, J. (2005) Cell-permeable near-infrared fluorogenic substrates for imaging β-lactamase activity. *J. Am. Chem. Soc. 127* (12), 4158−4159.
(55) Zhang, S., Metelev, V., Tabatadze, D., Zamecnik, P., and Bogdanov, A., Jr. (2008) Near-Infrared Fluorescent Oligodeoxyribonucleotide Reporters for Sensing NF-κB DNA Interactions In Vitro. *Oligonucleotides 18* (3), 235−243.
(56) Zou, P., and Ting, A. Y. (2011) Imaging LDL Receptor Oligomerization during Endocytosis Using a Co-internalization Assay. *ACS Chem. Biol. 6* (4), 308−313.
(57) Lovell, J. F., Jin, C. S., Huynh, E., MacDonald, T. D., Cao, W., and Zheng, G. (2012) Enzymatic Regioselection for the Synthesis and Biodegradation of Porphysome Nanovesicles. *Angew. Chem., Int. Ed. 51* (10), 2429−2433.
(58) He, C., Liu, D., and Lin, W. (2015) Self-Assembled Core-Shell Nanoparticles for Combined Chemotherapy and Photodynamic Therapy of Resistant Head and Neck Cancers. *ACS Nano 9* (1), 991−1003.
(59) Ng, K. K., Takada, M., Harmatys, K., Chen, J., and Zheng, G. (2016) Chlorosome-Inspired Synthesis of Templated Metallochlorin-Lipid Nanoassemblies for Biomedical Applications. *ACS Nano 10* (4), 4092−4101.
(60) Linder, K. E., Metcalfe, E., Nanjappan, P., Arunachalam, T., Ramos, K., Skedzielewski, T. M., Marinelli, E. R., Tweedle, M. F., Nunn, A. D., and Swenson, R. E. (2011) Synthesis, In Vitro Evaluation, and In Vivo Metabolism of Fluor/Quencher Compounds Containing IRDye 800CW and Black Hole Quencher-3 (BHQ-3). *Bioconjugate Chem. 22* (7), 1287−1297.
(61) Simard, B., Tomanek, B., van Veggel, F. C. J. M., and Abulrob, A. (2013) Optimal dye-quencher pairs for the design of an"“" "activatable"“" nanoprobe for optical imaging. *Photochem. Photobiol. Sci. 12* (10), 1824−1829.
(62) Uddin, M. I., Evans, S. M., Craft, J. R., Marnett, L. J., Uddin, M. J., and Jayagopal, A. (2015) Applications of Azo-Based Probes for Imaging Retinal Hypoxia. *ACS Med. Chem. Lett. 6* (4), 445−449.
(63) Varandas, P. A. M. M., Cobb, A. J. A., Segundo, M. A., and Silva, E. M. P. (2020) Emergent Glycerophospholipid Fluorescent Probes: Synthesis and Applications. *Bioconjugate Chem. 31* (3), 417−435.
(64) Egusquiaguirre, S. P., Igartua, M., Hernandez, R. M., and Pedraz, J. L. (2012) Nanoparticle delivery systems for cancer therapy: advances in clinical and preclinical research. *Clin. Transl. Oncol. 14* (2), 83−93.
(65) Anikeeva, N., Sykulev, Y., Delikatny, E. J., and Popov, A. V. (2014) Core-based lipid nanoparticles as a nanoplatform for delivery of near-infrared fluorescent imaging agents. *Am. J. Nucl. Med. Mol. Imaging 4* (6), 507−524.
(66) Allen, T. M., Hansen, C., Martin, F., Redemann, C., and Yau-Young, A. (1991) Liposomes containing synthetic lipid derivatives of polyethylene glycol show prolonged circulation half-lives in vivo. *Biochim. Biophys. Acta, Biomembr. 1066* (1), 29−36.
(67) Jhaveri, A. M., and Torchilin, V. P. (2014) Multifunctional polymeric micelles for delivery of drugs and siRNA. *Front. Pharmacol. 5*, 1−26.
(68) Szebeni, J., and Barenholz, Y. (2012) Complement activation, immunogenicity, and immune suppression as potential side effects of liposomes, in *Handbook of Harnessing Biomaterials in Nanomedicine* (Peer, D., Ed.) pp 309−334, 2 plates, Pan Stanford Publishing Pte. Ltd.
(69) Ramoni, C., Spadaro, F., Barletta, B., Dupuis, M. L., and Podo, F. (2004) Phosphatidylcholine-specific phospholipase C in mitogen-stimulated fibroblasts. *Exp. Cell Res. 299* (2), 370−382.
(70) Shin, H., Kwak, M., Lee, T. G., and Lee, J. Y. (2020) Quantifying the level of nanoparticle uptake in mammalian cells using flow cytometry. *Nanoscale 12* (29), 15743−15751.
(71) Illien, F., Rodriguez, N., Amoura, M., Joliot, A., Pallerla, M., Cribier, S., Burlina, F., and Sagan, S. (2016) Quantitative fluorescence spectroscopy and flow cytometry analyses of cell-penetrating peptides internalization pathways: optimization, pitfalls, comparison with mass spectrometry quantification. *Sci. Rep. 6*, 36938.
(72) Liao-Chan, S., Daine-Matsuoka, B., Heald, N., Wong, T., Lin, T., Cai, A. G., Lai, M., D'Alessio, J. A., and Theunissen, J.-W. (2015) Quantitative assessment of antibody internalization with novel monoclonal antibodies against alexa fluorophores. *PLoS One 10* (4), No. e0124708.
(73) Chan, S. Y. V., Hilchie, A. L., Brown, M. G., Anderson, R., and Hoskin, D. W. (2007) Apoptosis induced by intracellular ceramide accumulation in MDA-MB-435 breast carcinoma cells is dependent on the generation of reactive oxygen species. *Exp. Mol. Pathol. 82* (1), 1−11.
(74) Lovell, J. F., Chen, J., Jarvi, M. T., Cao, W.-G., Allen, A. D., Liu, Y., Tidwell, T. T., Wilson, B. C., and Zheng, G. (2009) FRET Quenching of Photosensitizer Singlet Oxygen Generation. *J. Phys. Chem. B 113* (10), 3203−3211.
(75) Lovell, J. F., Chan, M. W., Qi, Q., Chen, J., and Zheng, G. (2011) Porphyrin FRET Acceptors for Apoptosis Induction and Monitoring. *J. Am. Chem. Soc. 133* (46), 18580−18582.
(76) Dehghani, H., Eames, M. E., Yalavarthy, P. K., Davis, S. C., Srinivasan, S., Carpenter, C. M., Pogue, B. W., and Paulsen, K. D. (2009) Near infrared optical tomography using NIRFAST: Algorithm for numerical model and image reconstruction. *Commun. Numer Methods Eng. 25* (6), 711−732.
(77) Ban, H. Y., Busch, D. R., Pathak, S., Moscatelli, F. A., Machida, M., Schotland, J. C., Markel, V. A., and Yodh, A. G. (2013) Diffuse optical tomography in the presence of a chest wall. *J. Biomed. Opt. 18* (2), 26016.
(78) Ban, H. Y., Kavuri, V. C., Cochran, J. M., Pathak, S., Chung, S. H., Yodh, A. G., Schweiger, M., Arridge, S. R., Xie, L., Busch, D. R., et al. (2016) Heterodyne frequency-domain multispectral diffuse optical tomography of breast cancer in the parallel-plane transmission geometry. *Med. Phys. 43* (7), 4383.

https://doi.org/10.1021/acs.bioconjchem.1c00295
Bioconjugate Chem. 2021, 32, 1852−1863